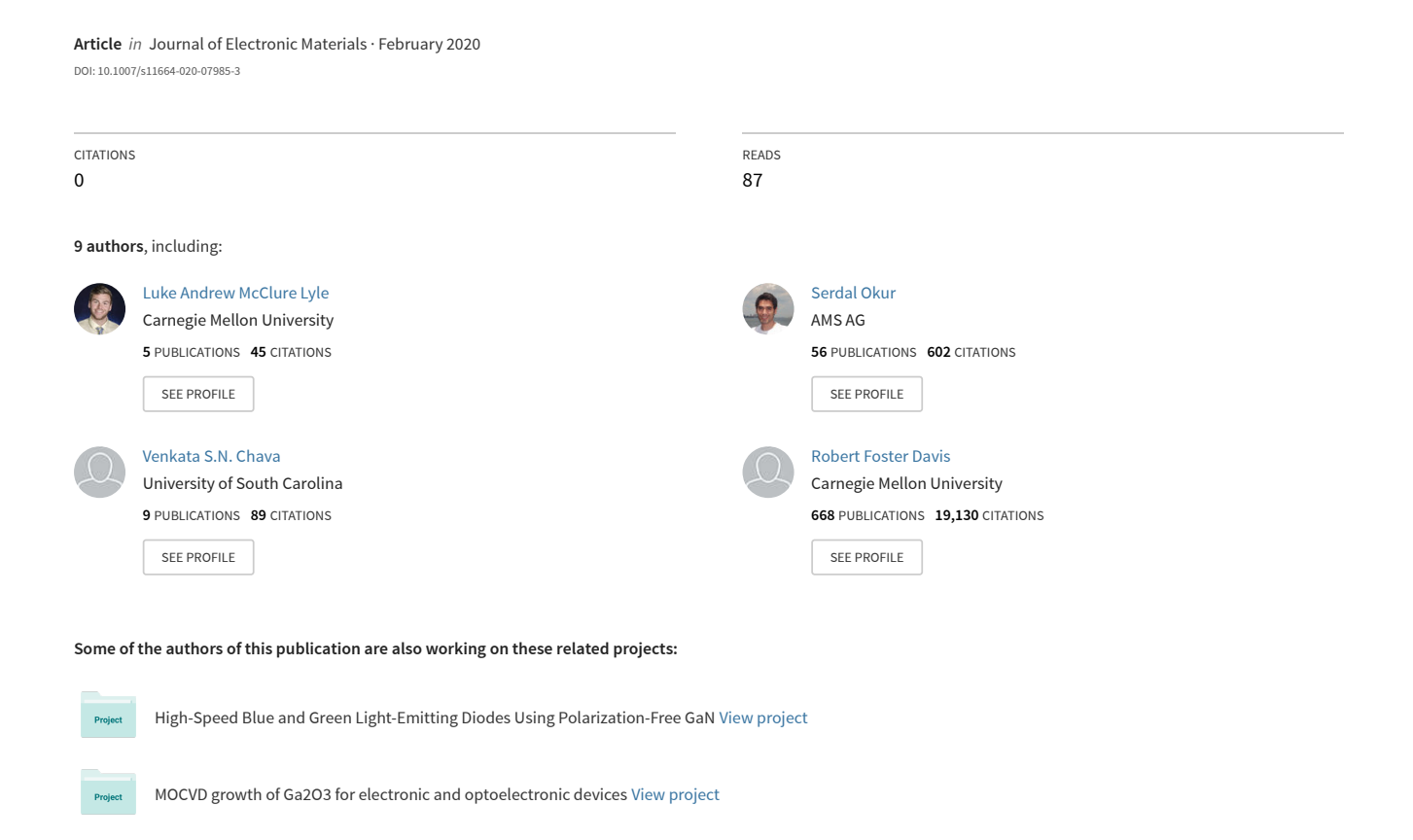
# Characterization of Epitaxial $\beta$ -(Al,Ga,In)2O3-Based Films and Applications as UV Photodetectors



## Check for updates

#### TOPICAL COLLECTION: 61ST ELECTRONIC MATERIALS CONFERENCE 2019

# Characterization of Epitaxial $\beta$ -(Al,Ga,In)<sub>2</sub>O<sub>3</sub>-Based Films and Applications as UV Photodetectors

LUKE A.M. LYLE  $^{\circ}$ ,  $^{1,5}$  SERDAL OKUR,  $^2$  VENKATA S.N. CHAVA,  $^3$  MATHEW L. KELLEY,  $^4$  ROBERT F. DAVIS,  $^1$  GARY S. TOMPA,  $^2$  M.V.S. CHANDRASHEKHAR,  $^3$  ANDREW B. GREYTAK,  $^4$  and LISA M. PORTER  $^{\circ}$ 

1.—Department of Materials Science and Engineering, Carnegie Mellon University, Pittsburgh, PA, USA. 2.—Structured Materials Industries, Inc., Piscataway, NJ, USA. 3.—Department of Electrical Engineering, University of South Carolina, Columbia, SC, USA. 4.—Department of Chemistry and Biochemistry, University of South Carolina, Columbia, SC, USA. 5.—e-mail: llyle@andrew.cmu.edu

Epitaxial films of  $\beta$ -(Al $_x$ Ga $_{1-x}$ ) $_2$ O $_3$ ,  $\beta$ -Ga $_2$ O $_3$ , and  $\beta$ -(In $_x$ Ga $_{1-x}$ ) $_2$ O $_3$  were grown on (001) sapphire substrates via metalorganic chemical vapor deposition (MOCVD). The compositions of the films as determined from energy dispersive x-ray analysis (EDX) and x-ray photoelectron spectroscopy (XPS) results were  $X_{\rm Al}$  = 0.57  $\pm$  0.05 and 0.76  $\pm$  0.05 and  $X_{\rm In}$  = 0.12  $\pm$  0.05 and 0.21  $\pm$  0.05. The optical bandgap was found to correspondingly vary between  $6.0 \pm 0.2$  and 3.9± 0.1 eV, as a function of composition via XPS and UV-visible spectroscopy (UV-Vis). X-ray diffraction, scanning electron microscopy, and atomic force microscopy revealed the films to be highly-oriented ( $\bar{2}01$ )-epitaxial films with nanocrystalline domains. Schottky- and MSM-based solar-blind UV photodetectors were fabricated on the films and showed responsivities at 20 V varying from  $> 10^4$  A/W for the  $Ga_2O_3$  devices,  $> 10^3$  A/W for the  $(Al_rGa_{1-r})_2O_3$  devices and  $> 10^2$  A/W for the  $(In_xGa_{1-x})_2O_3$  devices. Modest shifts in wavelength selectivity corresponding with the changes in composition/bandgap were also measured. Time response measurements on Schottky and MSM detectors reveal rise and dwell times on the order of a minute, indicating the presence of photoconductive gain. Noise-equivalent powers were in the fW-pW regime with specific detectivities  $(D^*)$  between  $10^{10}$  and  $10^{12}$  Jones. Scanning photocurrent maps display large photocurrent generation at the Schottky interface in the case of a  $\beta$ -Ga<sub>2</sub>O<sub>3</sub> Schottky detector, whereas for an  $\beta$ -(In-<sub>x</sub>Ga<sub>1-x</sub>)<sub>2</sub>O<sub>3</sub> MSM detector the photocurrent generation occurs in the device channel and at the Schottky interface.

**Key words:**  $\beta$ -(Al<sub>x</sub>Ga<sub>1-x</sub>)<sub>2</sub>O<sub>3</sub>,  $\beta$ -Ga<sub>2</sub>O<sub>3</sub>,  $\beta$ -(In<sub>x</sub>Ga<sub>1-x</sub>)<sub>2</sub>O<sub>3</sub>, Metalorganic chemical vapor deposition

#### INTRODUCTION

UV photodetectors are of high interest to numerous industries and the military for applications ranging from flame- and missile-plume detection to ozone hole monitoring. Due to its ultrawide bandgap,  $Ga_2O_3$  is well suited for UV photodetectors that are solar-blind and therefore insensitive to wavelengths greater than  $\sim 280$  nm. The ability to grow single crystals of  $\beta$ -Ga $_2O_3$  from various liquid-phase methods  $^{1-6}$  provides further practical advantage for the use of this semiconductor.

In<sub>2</sub>O<sub>3</sub>, Ga<sub>2</sub>O<sub>3</sub>, and Al<sub>2</sub>O<sub>3</sub>, which have bandgaps of 2.7, 4.6 and 9 eV, respectively, form the basis of a

(Received September 16, 2019; accepted January 30, 2020)

Published online: 11 February 2020

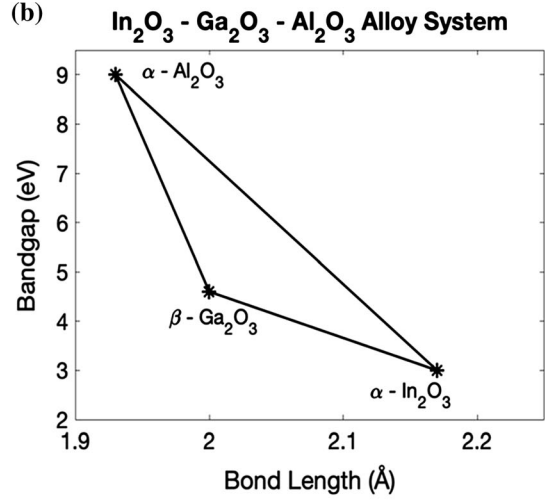
Group III-oxide alloy system (Fig. 1b). As such, the to tune the bandgap potential  $\mathbf{exists}$ (Al,Ga,In)<sub>2</sub>O<sub>3</sub>-based alloys over a large energy range and, correspondingly, tune the wavelength selectivity of photodetectors based on these alloys. However, the binary oxides have different equilibrium crystal structures, which means that a phase change will occur at a certain composition within any of the ternary alloys. This study reports results on epitaxial films of  $Ga_2O_3$  and ternary  $(Al_x$  $Ga_{1-x})_2O_3$  and  $(In_xGa_{1-x})_2O_3$  alloys that remain within the  $\beta$  phase. We characterize their microstructural, chemical, and optical properties as a function of composition, and measure the photoresponse, time response, and noise spectra of metal-semiconductor-metal (MSM) and Schottky photodetectors based on these films. The results indicate bandgap tunability of  $\sim 1.5 \; \text{eV}$  for the compositions grown. Photodetectors with the highest responsivities for their respective material types are reported.

#### **EXPERIMENTAL**

 $Ga_2O_3$ ,  $(Al_xGa_{1-x})_2O_3$ , and  $(In_xGa_{1-x})_2O_3$  epitaxial films were grown on (001) c-plane sapphire substrates using metalorganic chemical vapor deposition (MOCVD). The MOCVD system (Fig. 1a) comprised a quartz vertical showerhead above a 2-inch stage. Gases flowed from above incident on the substrate where the samples were resistively heated.

Five epitaxial films were investigated in this study; one  $Ga_2O_3$  (GO-1), two  $(Al_xGa_{1-x})_2O_3$ (AlGO-1 and AlGO-2), and two  $(In_xGa_{1-x})_2O_3$ (InGO-1 and InGO-2). The films were deposited using an in-house custom-built MOCVD system consisting of a cylindrical quartz reactor (with two inlets at the top for the precursors: one for metalorganic precursor injection and the other for injection of oxygen), a gas delivery system and a vacuum system connected through flanges. All films were grown at 100 Torr with an Ar carrier gas. The chamber was evacuated with the use of a mechanical pump. The substrates were placed on the sample stage (Hastelloy susceptor) and were heated using an induction heating arrangement. The susceptor temperature was measured using an optical pyrometer. Once the growth temperature was reached, the precursors were introduced into the reactor through the gas inlets. The flow of the precursor gases to the quartz chamber was controlled using mass flow controllers calibrated for each gas. Over the course of the work a variety of process parameters were explored. Small variations in the process parameters (gas phase precursor flow rate) and substrate temperature affect the resulting film composition, which in turn will vary the composition, bandgap, and conductivity. For example, changing the precursor supply ratio at a fixed temperature changes the grown film alloy composition; changing the temperature does the same. The precursors also react differently with oxidizer species, and gas phase reactions tend to increase concentration and with thus can cause





(	(	•	1	١
'	•	_	1	

Sample	T(°C)	P(kPa)	TEGa(sccm)	TMAl/TMIn(sccm)	TeOS(sccm)	$O_2(sccm)$	Rate(nm/hr)	Thickness(nm)
GO-1	800	13.33	20	-	5	225	250	250
AlGO-1	800	13.33	80	10	-	225	750	750
AlGO-2	800	13.33	80	10	5	225	750	750
InGO-1	600	13.33	80	20	-	90	250	250
InGO-2	600	13.33	80	20	5	225	350	350

Fig. 1. (a) MOCVD growth setup used to grow  $Ga_2O_3$ ,  $(Al_xGa_{1-x})_2O_3$ , and  $(ln_xGa_{1-x})_2O_3$  films at Structured Materials Industries, Inc. (SMI). (b) Diagram illustrating the bandgaps and differences in bond length (i.e., structural mismatch) of thermodynamically stable phases of  $Ga_2O_3$ ,  $Al_2O_3$ , and  $In_2O_3$ . (c) Growth conditions for  $Ga_2O_3$ ,  $(Al_xGa_{1-x})_2O_3$ , and  $(In_xGa_{1-x})_2O_3$  films in this study.

homogeneous reactions in the gas phase that can reduce film growth rates and/or produce particles that may be incorporated into the growing film. We did not systematically study these complex interrelationships for these films. The Ga<sub>2</sub>O<sub>3</sub> (GO) and (Al<sub>x</sub>Ga<sub>1-x</sub>)<sub>2</sub>O<sub>3</sub> (AlGO) films reported in this study were grown at 800°C, whereas the (In<sub>x</sub>Ga<sub>1-x</sub>)<sub>2</sub>O<sub>3</sub> (InGO) films were grown at 600°C and annealed in ambient air at 800°C (the growth temperature of the GO and AlGO films) for 1 h to crystallize the films. The metalorganic sources triethyl gallium (TEG), trimethyl aluminum (TMA), and trimethyl indium (TMIn) and tetra orthosilicate (TEOS) (for doping) were placed in bubblers. The bubbler systems were designed such that a carrier gas of Ar bubbled through the precursor and transported the vapors of the metalorganic source to the chamber. The growth conditions, growth rate, and thickness for each film are tabulated in Fig. 1c. All films were nonconductive when measured using Hall effect and four-point probe measurements.

The films were characterized structurally, chemically and optically using a variety of complementary techniques, including x-ray diffraction (XRD), scanning electron microscopy (SEM) with energy dispersive x-ray analysis (EDX), atomic force microscopy (AFM), optical transmittance in the UVvisible range, and x-ray photoelectron spectroscopy (XPS). XRD characterization was conducted using a Panalytical X'pert Pro MPD x-ray diffractometer with Cu-K $\alpha$  radiation ( $\lambda = 0.154$  nm). Scans were obtained in the  $\theta$ -2 $\theta$  geometry. Optical properties of the films were measured in the UV-visible ( $\sim 230$ -800 nm) range using an OLI 770 multichannel spectroradiometer. AFM was performed using a Solver Next II AFM/SPM with a Si tip in semicontact mode. The SEM imaging and EDX characterization were conducted using a Phillips XL30 Scanning Electron Microscope (SEM) at 10 keV using  $K\alpha$  emission lines. The mole fractions ( $X_{Al}$  or  $X_{In}$ ) of InGO and AlGO films were calculated from EDX measurements by taking the atomic percentage of Al or In and normalizing with respect to the atomic percentage of Ga. XPS was performed at the Swagelok Center for Surface Analysis of Materials (SCSAM), using a PHI Versaprobe 5000 Scanning xray Photoelectron Spectrometer with an Al Kα x-ray source with a spot size of 100  $\mu$ m. The compositions of Al, Ga, In, and O were calculated by using the area under the high-resolution curves (Fig. 2) and weighted with the respective sensitivity factors for each elemental species. These atomic percentages were used to determine the mole fraction,  $X_{Al}$  or  $X_{In}$ , of AlGO and InGO films, respectively. Prior to the XPS measurements the samples were etched *in-situ* with a 3 kV Ar beam for 2 min to remove contaminants from the top  $\sim 20$  nm from the surface.

Photodetectors comprising 48 interdigitated contact fingers with nominal 50  $\mu$ m finger widths and finger spacings and an area of 0.625 cm<sup>2</sup> were fabricated using a standard photolithography

process. Prior to the photolithography process the samples were ultrasonicated in acetone, isopropyl alcohol, and deionized water for 10 min each. Two layers were spin-coated on the samples prior to patterning: a layer of hexamethyldisilazane (HMDS) to form an adhesion layer on the surface, and AZ 4210 photoresist. The samples were subsequently exposed to UV light for 1 min prior to developing the resist. Schottky detectors were fabricated comprising Ti/Au (20 nm/50 nm) ohmic contacts and 5-nm-thick Ni Schottky contacts. Metalsemiconductor-metal (MSM) photodetectors comprised two symmetrical 5-nm-thick Ni Schottky contacts. All contact metals were deposited via electron-beam evaporation in an ultra-high vacuum system. The ohmic contacts were annealed at 400°C for 5 min in an Ar atmosphere prior to deposition of the Schottky contacts.

The photoresponse measurements were performed using a monochromator with a Xe-arc lamp source, with  $P_{\rm opt}$  measured down to  $\sim$  200 nm at a slit-width of 10 nm using a Thorlabs UV-enhanced Si photodiode. The light was illuminated from the top of the device at a 45° angle, with a spot size of  $\sim$  1 cm². The photocurrent was then measured and normalized to the beam power. The extracted relative responsivity was calibrated to a broad area hand-held 254 nm Hg-vapor lamp with a uniform illumination density at 6.5  $\mu$ W/cm², comparable to the power in the monochromator beam at 254 nm to obtain an absolute  $R(\lambda)$ . The I–V measurements in the dark and under illumination were performed using an HP4155C parameter analyzer with a probe station.

The noise and transient measurements were performed with a Keithley 2610 2-channel sourcemeter to bias the device, with the device source routed into a current trans-impedance pre-amplifier whose input functioned as a virtual ground to measure the drain current  $I_D$ , which was also monitored using the source-meter. The output voltage was fed into an oscilloscope where the time dependence of current under 250 nm illumination was measured. In the dark, the drain current was allowed to stabilize for 5 min before taking data. The time trace of the dark current was converted to a frequency dependence using the FFT function on the oscilloscope, enabling measurement of the dark noise spectrum between 1 and 50 Hz. Scanning photocurrent maps (SPCM) were generated with illumination of a 444 nm laser, a chopper frequency of 113 Hz, and a bias of 500 mV with a resolution of  $1 \mu m$ .

### RESULTS

XPS and EDX measurements were employed as complementary tools for estimation of film compositions. Figure 2 shows high-resolution Ga  $2p_{3/2}$ , Al 2p, and In  $3d_{5/2}$  XPS peaks from respective films. Small differences in the Al 2p and In 3d peak

positions between samples could be due to the different compositions and therefore different bonding arrangements of the atoms, as well as differences in surface band bending; some charging due to the nonconductive sapphire substrate could also affect the binding energy positions. As mentioned in the Experimental section, the compositions as estimated from XPS measurements were calculated using peak areas rather than the precise peak positions. The estimated compositions from XPS were  $X_{\rm In}=0.20$  and 0.11 for  $({\rm In}_x{\rm Ga}_{1-x})_2{\rm O}_3$  in InGO-1 and InGO-2, respectively. For the AlGO films, XPS yielded estimated compositions of  $X_{\rm Al}=0.76$  and 0.59 for  $({\rm Al}_x{\rm Ga}_{1-x})_2{\rm O}_3$  in AlGO-1 and AlGO-2, respectively.

Film compositions were also estimated from EDX measurements. EDX yielded estimated compositions of  $X_{\rm In} = 0.21$  and 0.12 for  $({\rm In}_x{\rm Ga}_{1-x})_2{\rm O}_3$  in InGO-1 and InGO-2, respectively. For AlGO-1 and AlGO-2, EDX yielded an estimated composition of  $X_{\rm Al} = 0.66$  and 0.54 in  $({\rm Al}_x{\rm Ga}_{1-x})_2{\rm O}_3$ , respectively.

Optical transmittance and reflectance measurements were conducted to determine the optical properties and bandgaps of the films. Figure 3a displays the normalized transmittance of GO-1, AlGO-2, InGO-1, and InGO-2. Transmittance and

reflectance data can be used to determine the bandgaps by the Tauc relation:<sup>8</sup>

$$(\alpha h v)^2 = A(h v - E_G), \tag{1}$$

where  $\alpha = -\frac{1}{d} \ln \frac{T}{1-R}$ , T is the transmittance, R is the reflectance, and d is the film thickness. Extrapolation of the curve for GO-1 yields a bandgap of  $4.6 \pm 0.1 \, \mathrm{eV}$ , which is within the range reported for  $\beta\text{-Ga}_2\mathrm{O}_3$ . Similarly, InGO-1 and InGO-2 samples yield bandgaps of  $3.8 \pm 0.1 \, \mathrm{eV}$  and  $4.0 \pm 0.1 \, \mathrm{eV}$ , respectively. The wavelength (energy) range of our OLI 770 multichannel spectroradiometer was insufficient to extrapolate a bandgap value for AlGO-2 although it is apparent from the curve that the bandgap shifts to higher energy.

XPS was used as a complementary method to estimate bandgap values. Bandgaps were calculated from XPS measurements by taking the difference between the onset of inelastic losses before the elastic Ga  $2p_{3/2}$  peak and the core level of the elastic Ga  $2p_{3/2}$  peak. A linear extrapolation is performed before the onset of inelastic losses, occurring at a slightly higher energy than the given elastic peak, to where the onset of inelastic losses reaches a minimum; the difference between the onset of inelastic losses and the core energy level of the

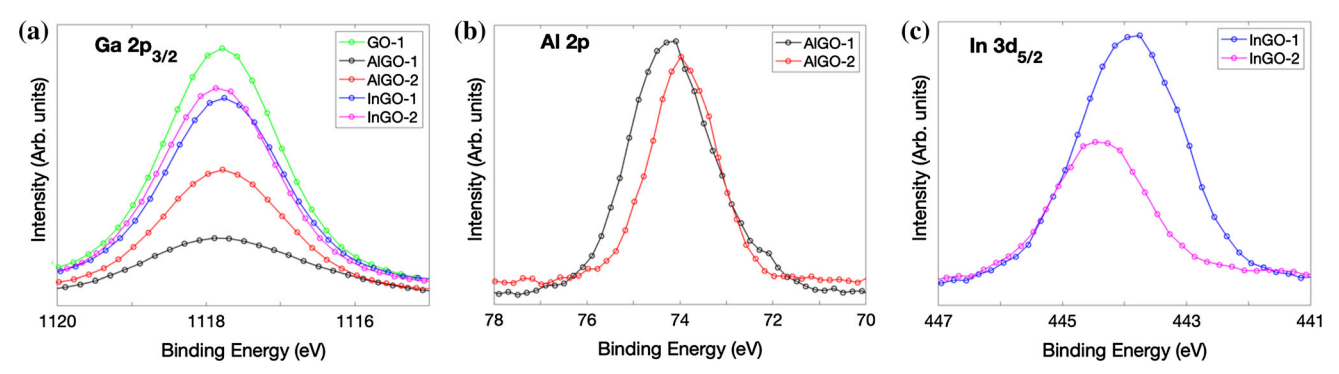


Fig. 2. High-resolution XPS scans of (a) the Ga  $2p_{3/2}$  peak, (b) the Al 2p in  $(Al_xGa_{1-x})_2O_3$  films. (c) the In  $3d_{5/2}$  peak in  $(In_xGa_{1-x})_2O_3$  films.

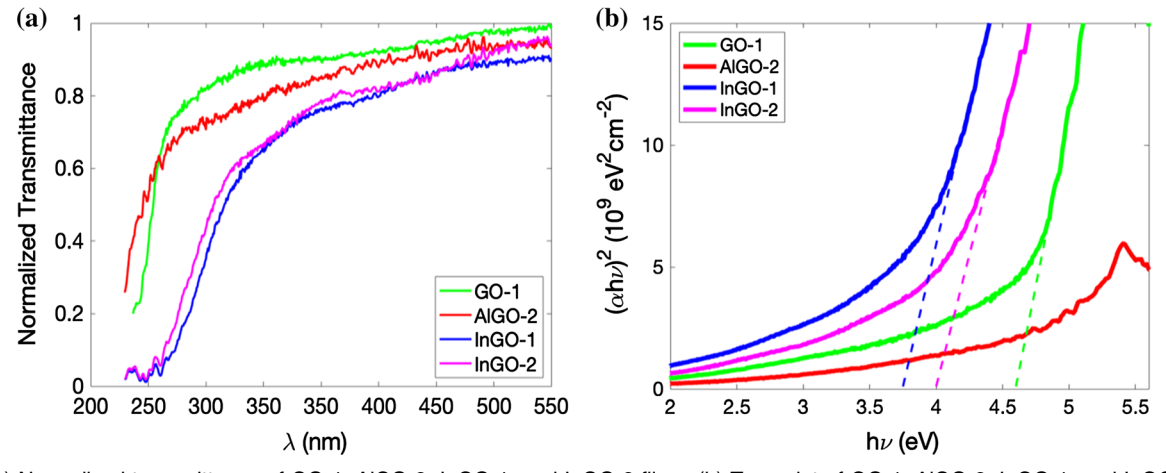


Fig. 3. (a) Normalized transmittance of GO-1, AIGO-2, InGO-1, and InGO-2 films. (b) Tauc plot of GO-1, AIGO-2, InGO-1, and InGO-2 films.

peak is equated to the bandgap. This method of estimating band gaps provides an alternative to optical measurements, for which most setups are limited to wavelengths  $\geq 200$  nm and therefore not useful for measuring band gaps  $\sim 6$  eV or greater. The XPS-determined bandgap values for GO-1, InGO-1, InGO-2, AlGO-1 and AlGO-2 were found to be  $4.6\pm0.2$  eV,  $4.0\pm0.2$  eV,  $4.2\pm0.2$ , eV,  $6.0\pm0.2$  eV, and  $5.6\pm0.2$  eV, respectively, which are in close agreement with the respective Tauc-plot values.

XRD was performed to identify the crystal structure and phases of the films. Figure 4a displays  $\theta-2\theta$  scans for  $2\theta=15^{\circ}-85^{\circ}$ .  $Ga_2O_3$  displays a set of  $\beta$ -  $Ga_2O_3$  (201) peaks, typical for  $Ga_2O_3$  films grown on (001) sapphire. The  $(In_xGa_{1-x})_2O_3$  and  $(Al_xGa_{1-x})_2O_3$  films displayed peaks near the  $\{\overline{2}01\}$   $Ga_2O_3$  peaks but shifted slightly to lower and higher angles, respectively. The small shifts to lower (higher) angles shown in Fig. 4b are attributed to a small increase (decrease) in the lattice parameter associated with In (Al) incorporation,  $^{9,12-15}$  and further indicate that these epitaxial alloy films are  $\beta$ -phase (201)-oriented. The films also displayed a minor peak at 20.4° that could not be identified. In contrast, for reasons that have not been determined,

AlGO-1 was primarily amorphous. Composition estimations from these peak shifts would require higher resolution XRD measurements and a comprehensive XRD analysis of standard references.

Figure 4c, d and e show representative SEM (left) and AFM (right) images of GO-1, InGO-1, and AlGO-2, films. From the images we estimate that GO-1 is comprised of in-plane rotational domains  $\sim 100-200$  nm in size; similar domains  $\sim 300-400$  nm and  $\sim 600-800$  nm appear to be present in the AlGO-2 and InGO-2 films, respectively.

Figure 5 summarizes the compositions and bandgap values determined from the characterizations of  $\beta\text{-}(\mathrm{Al}_x\mathrm{Ga}_{1-x})_2\mathrm{O}_3$  and  $\beta\text{-}(\mathrm{In}_x\mathrm{Ga}_{1-x})_2\mathrm{O}_3$  described above. The plot shows the bandgap values plotted as a function of incorporated In and Al, as determined in this study, and compares them with bandgap values from the literature for films grown by other methods. The bandgap values in this study span  $\sim 1.5$  eV for  $\beta\text{-}(\mathrm{Al},\mathrm{Ga},\mathrm{In})_2\mathrm{O}_3$  films and are mostly in agreement with other reported values, although there is some difference for the  $(\mathrm{In}_x\mathrm{Ga}_{1-x})_2\mathrm{O}_3$  compositions. The differences could be due to uncertainty in the compositions estimated in previously reported films or due to microstructural influences from these nanocrystalline films.

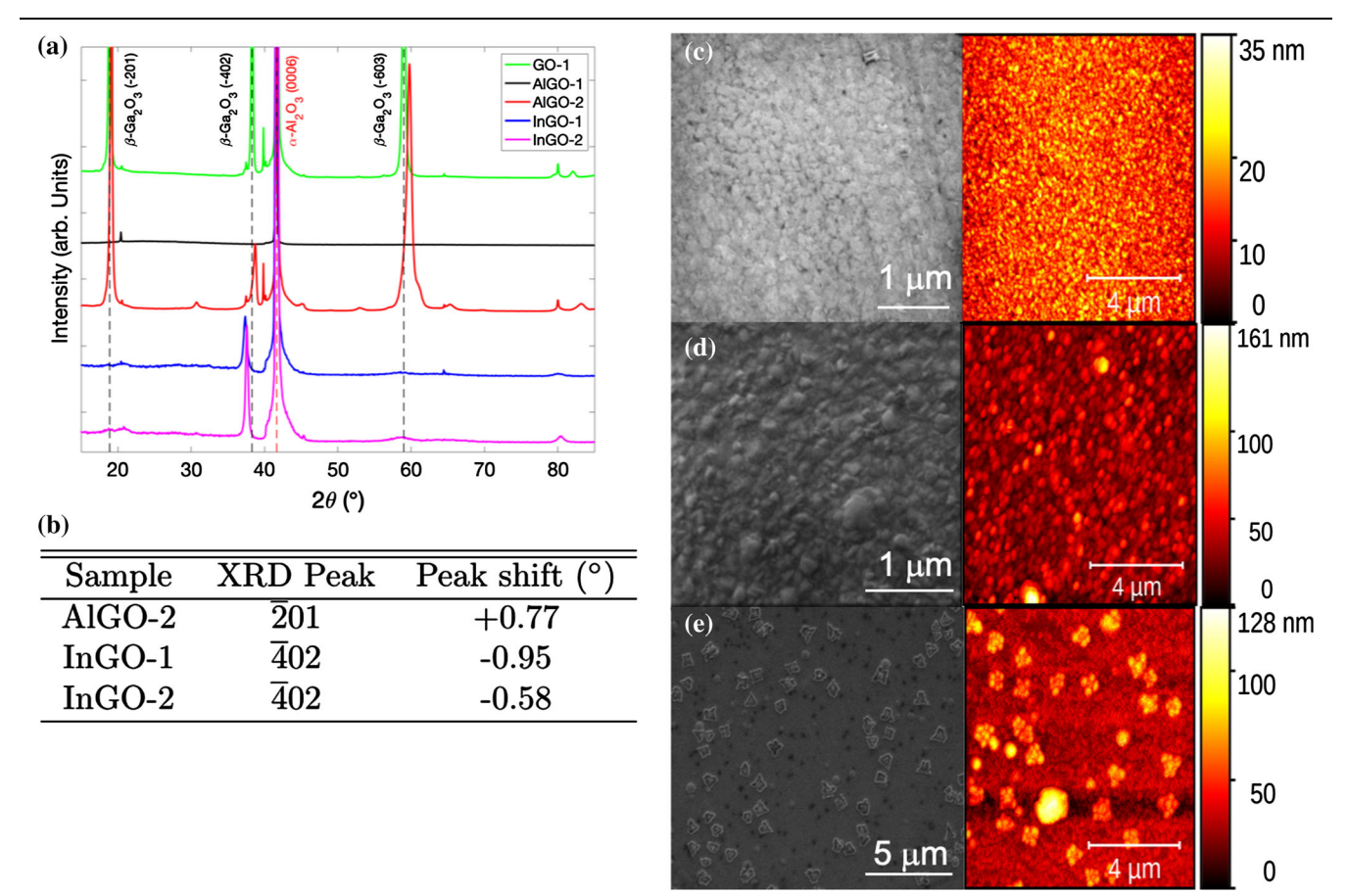


Fig. 4. (a) Survey XRD scans showing preferred  $(\bar{2}01)$  orientation for  $Ga_2O_3$ ,  $(Al_xGa_{1-x})_2O_3$ , and  $(In_xGa_{1-x})_2O_3$  growth on c-plane sapphire substrates. (b) Shift of XRD peaks to the right for crystalline AlGO-2 and to the left for InGO-1 and InGO-2. SEM (left) and AFM (right) of (c) GO-1, (d) AlGO-2, and (e) InGO-1 films.

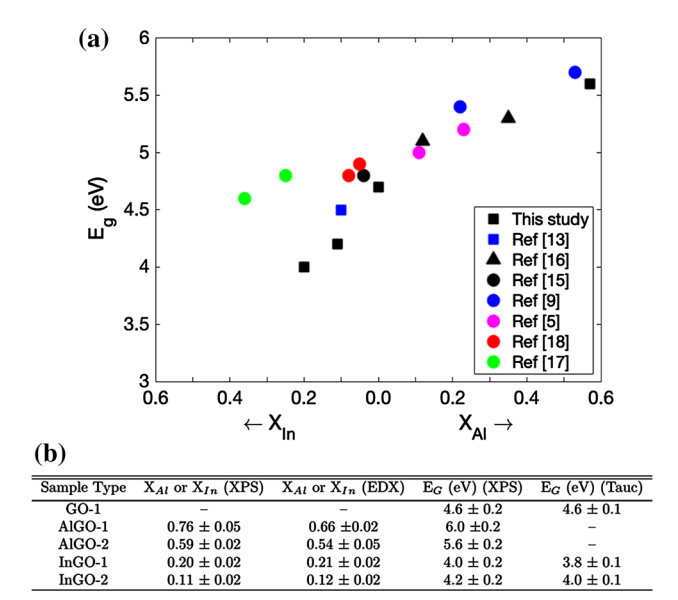


Fig. 5. (a) Bandgap versus composition for other  $\beta$ -(Al $_x$ Ga $_{1-x}$ ) $_2$ O $_3$ , and  $\beta$ -(In $_x$ Ga $_{1-x}$ ) $_2$ O $_3$  Squares represent MOCVD growth, triangles represent MBE growth and circles represent PLD growth. (b) Table displaying the results of the bandgaps and compositions obtained from XPS, EDX and Tauc plots for the Ga $_2$ O $_3$ , (Al $_x$ Ga $_{1-x}$ ) $_2$ O $_3$ , and (In $_x$ Ga $_{1-x}$ ) $_2$ O $_3$  films.

The remaining experiments describe the results of photodetectors that were fabricated from each of the five films described above. MSM photodetectors based on  $\beta$ -(Al<sub>x</sub>Ga<sub>1-x</sub>)<sub>2</sub>O<sub>3</sub> films with lower Al-con $tent^{5,9,16}$  and  $\beta$ - $(In_xGa_{1-x})_2O_3$  ( $X_{In} = 0.05-0.36$ ) films  $^{13,15,17,18}$  have been reported previously. Figure 6a, b, and c shows the photoresponsivity as a function of wavelength for the working MSM detectors (at 12 V, forward bias) and Schottky detectors (at - 12 V, reverse bias) overlaid with the normalized film transmittance. Because only a few devices fit on each  $1 \times 1$  cm sample, some device types on certain samples did not work and are therefore not displayed in the plots. For GO-1 and AlGO-2 devices (Fig. 6a, b), the responsivity increases in accordance with the locations of relatively sharp absorption edges, as expected. For the  $(In_xGa_{1-x})_2O_3$  detectors the transmittance and the photoresponse also increase at approximately the same location, but the transmittance curve increases more gradually, suggestive of an indirect bandgap (Fig. 6c). Figure 6d shows the responsivity of a detector from each film, normalized to the maximum response of the respective detector. A wavelength shift of  $\sim 30 \text{ nm}$  from lower to higher wavelengths is observed for the  $(Al_xGa_{1-x})_2O_3$ , and  $(In_xGa_{1-x})_2O_3$ photodetectors, respectively. With respect to device performance, the peak responsivity values are shown in a table in Fig. 7d. To our knowledge these values are the largest responsivities reported for  $Ga_2O_3$  thin film detectors,  $(Al_xGa_{1-x})_2O_3$  photodetectors, and  $(In_xGa_{1-x})_2O_3$  photodetectors to date.

Figure 7a, b shows rise and dwell times for the devices in response to 250 nm light. Figure 7e tabulates the rise times measured by taking the

difference between the times where the current reaches 10% of its value and when the current reaches 90% of its value under illumination. The dwell times are measured by taking the difference between the times where the current reaches 90% of its value and when the current reaches 10% of its value after the illumination is removed. The slow response time, with rise and dwell times on the order of a minute, coupled with ultrahigh responsivities point towards photoconductive gain being the contributing gain mechanism.

Such high responsivity values indicate the presence of photoconductive gain, as a quantum efficiency of 100%should yield much lower responsivities in this range. During illumination, instead of the UV light directly promoting an electron from the valence band to the conduction band, it could promote the electron to a trap state. In trap states, emptying and filling occurs slowly and, depending on the number of these trap states, their energy level, and their density, they can serve to substantially increase the time response of detectors. Photoconductive gain was observed in  $Ga_2O_3$  by Armstrong et al. 19 in an EFG Tamura substrate. The gain was attributed to self-trapped holes (STHs) in the depletion region. STHs, which are effectively immobile positive charges that occur in  $\beta$ -Ga<sub>2</sub>O<sub>3</sub> due to local deformation potentials in the lattice, can drastically increase the hole recombination time in devices.<sup>20,21</sup>

Figure 7c displays the noise power density for the measured devices. Measured noise power density,  $S_n(f)$ , can be converted into total noise current,  $i_n^2$ :

$$\langle i_n^2 \rangle = \int_0^B S_n(f) \mathrm{d}f.$$
 (2)

Because these detectors are very slow, an adequate  $i_n^2$  can be calculated using a bandwidth,  $B=1~\mathrm{Hz}.$ 

Noise equivalent power (NEP) is the smallest optical power that can be detected for a given noise level, and is given by:

$$NEP = \frac{\sqrt{\langle i_n^2 \rangle}}{R}, \qquad (3)$$

where R is the peak responsivity in A/W. The frequency dependence of the GO-1 Schottky and MSM detector is well fit with a  $1/f^2$  dependence, whereas the InGO-1 MSM, InGO-2 MSM and Schottky are well within a 1/f dependence. For detectors on InGO-1 and InGO-2 the 1/f trend diverges around 10 Hz as the devices go into the flatband condition. Similarly, for the GO-1 devices the MSM detector diverges from  $1/f^2$  around 10 Hz into a 1/f behavior, whereas the GO-1 Schottky detector diverges from  $1/f^2$  to 1/f around 20 Hz. 1/f noise, referred to as flicker noise or a fluctuation in conductivity, is attributed to distributed trap states

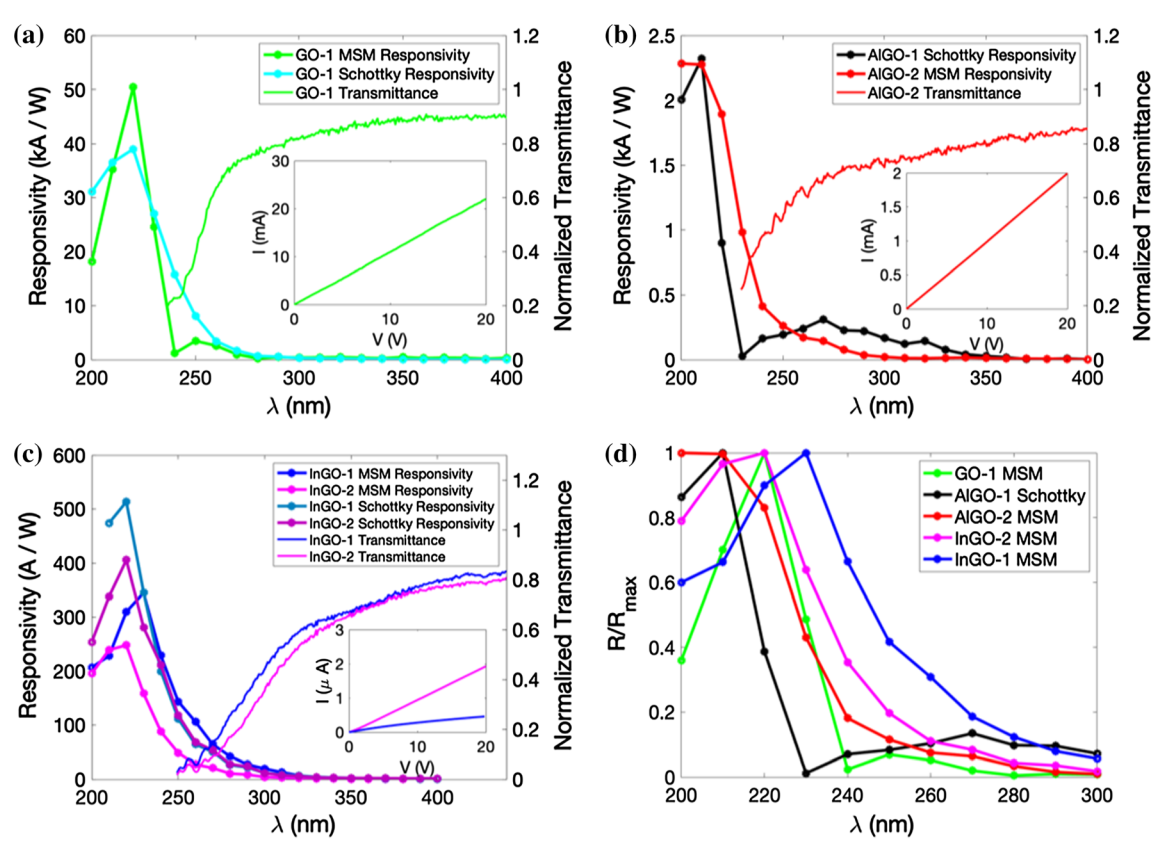


Fig. 6. (a) GO-1 MSM and Schottky detectors responsivity at 12 V overlaid with GO-1 normalized transmittance plotted as a function of wavelength with dark IV of GO-1 MSM (inset). (b) AIGO-1 Schottky and AIGO-2 MSM detectors responsivity at 12 V overlaid with AIGO-2 normalized transmittance plotted as a function of wavelength with dark IV of AIGO-2 MSM (inset). (c) InGO-1 MSM and Schottky and InGO-2 MSM and Schottky detectors responsivity at 12 V overlaid with InGO-1 and InGO-2 normalized transmittance plotted as a function of wavelength with dark IV of InGO-1 and InGO-2 MSM detectors (inset). (d) Responsivity of GO-1 MSM, AIGO-1 Schottky, AIGO-2 MSM, InGO-1 MSM, and InGO-2 MSM at 12 V normalized to their respective maximum values as a function of wavelength.

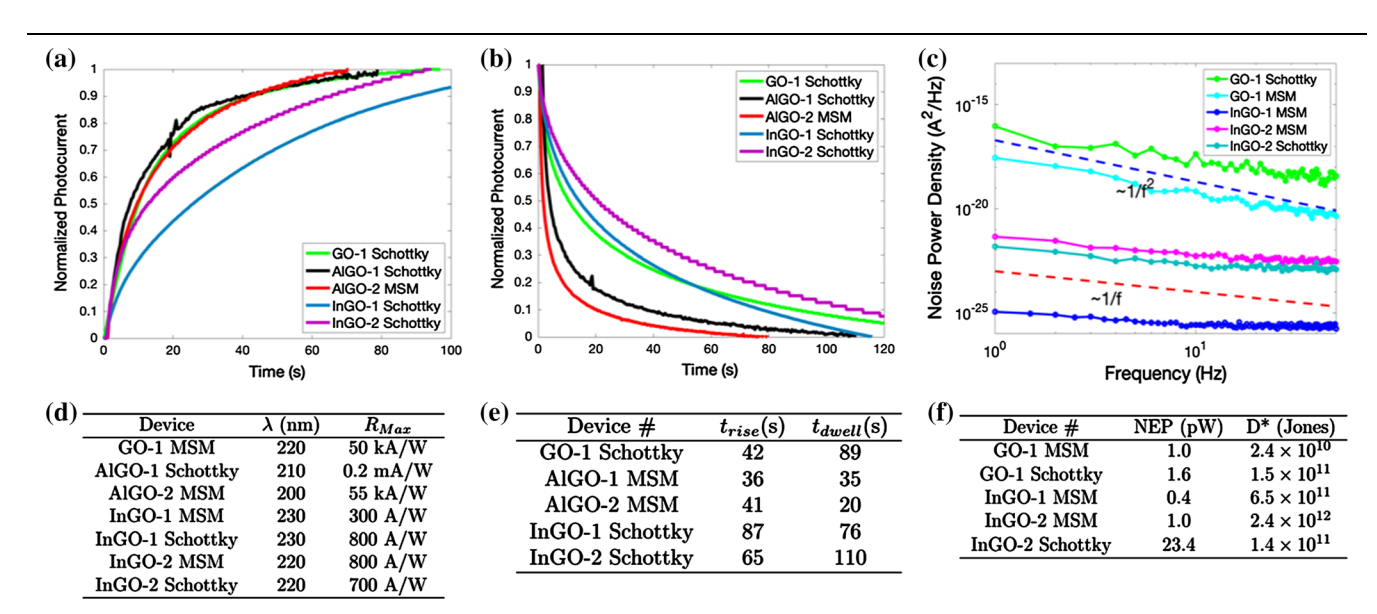


Fig. 7. (a) Normalized photocurrent when exposed to 250 nm light and (b) unexposed to 250 nm light for GO-1 Schottky, AlGO-1 MSM, AlGO-2 MSM, InGO-1 Schottky, and InGO-2 Schottky detectors. (c) Noise power density spectra of GO-1 Schottky and MSM, InGO-1 MSM, and InGO-2 Schottky and MSM as a function of frequency overlaid with 1/f and 1/f<sup>2</sup> trendlines between 1-50 Hz. (e) Rise and dwell times of GO-1 Schottky, AlGO-1 MSM, AlGO-2 MSM, InGO-1 Schottky, and InGO-2 Schottky detectors. (f) NEP and detectivity of GO-1 Schottky and MSM, InGO-1 MSM, and InGO-2 Schottky and MSM.

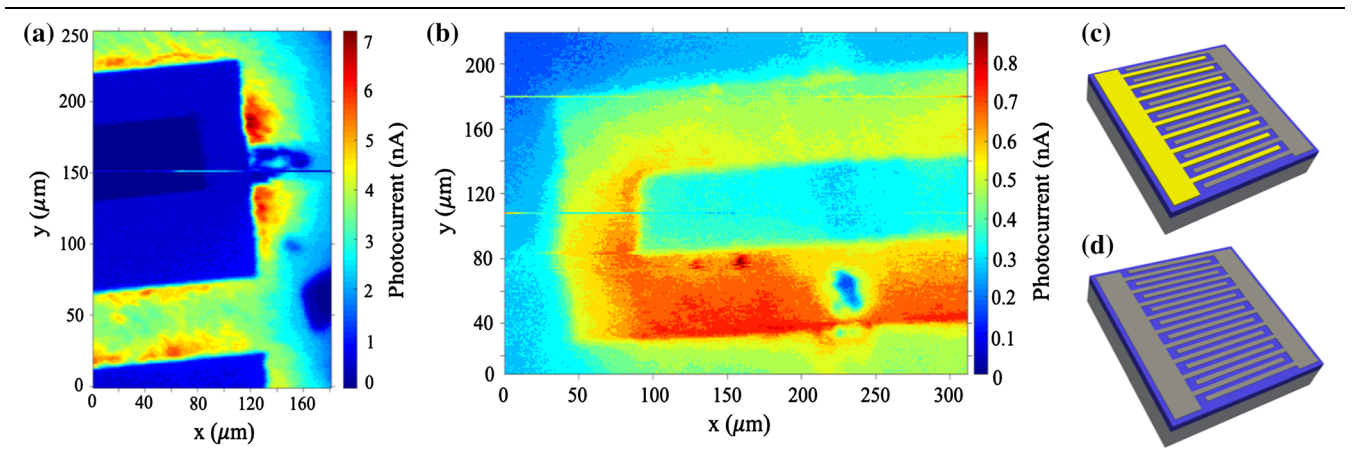


Fig. 8. SPCM of (a) GO-1 Schottky photodetector and (b) InGO-1 MSM photodetector. A laser using sub-bandgap (444 nm) light is rastered across the sample and the photocurrent is measured in the devices. Schematic of (c) Schottky photodetector with Ni–Ti/Au contacts and (d) MSM photodetector with Ni–Ni contacts.

throughout the bandgap, whereas  $1/f^2$  noise corresponds to discrete, highly populated trap states. These results therefore suggest discrete trap states in the GO devices and distributed trap states in the bandgap of the InGO devices.

The specific detectivity,  $D^*$ , describes the smallest detectable signal and is independent of area and bandwidth.  $D^*$  can be calculated by:

$$D^* = \frac{\sqrt{AB}}{NEP},\tag{4}$$

where A is the area. Figure 7f displays calculated NEP and  $D^*$  values. Our detectors have NEPs in the low pW-fW regime. To the best of the authors' knowledge, these NEP are the lowest reported for  $Ga_2O_3$  and  $(In_xGa_{1-x})_2O_3$  thin film detectors.

Scanning photocurrent maps (SPCM) were obtained for the GO-1 Schottky device (Fig. 8a) and the InGO-1 MSM device (Fig. 8b). In this technique a 444 nm laser rasters over a biased device and spatially measures the photocurrent. Figure 8a illustrates photocurrent generation at the semi-opaque ( $\sim 5$  nm) Ni Schottky metal on the GO-1 Schottky photodetector, where a photocurrent of 4–7 nA is observed. A smaller photocurrent of  $\sim 1$  nA was measured in the channel between the contacts. In contrast, for the InGO-1 MSM the photocurrent under the semi-opaque Ni contacts was smaller than the photocurrent measured in the channel.

The high responsivity, slow time response, and SPCM of our GO-1 Schottky detector provide strong evidence that the gain mechanism provided in  $\beta$ -Ga<sub>2</sub>O<sub>3</sub> photodetectors is due to interfacial trapping. The boundaries separating nanocrystalline domains within the films would give a higher density of dangling bonds that act as surface trap states for electrons/holes. However, there is very little photocurrent generated in the GO-1 Schottky channel (Fig. 8a), implying surface trap states cannot be a

dominating effect in the gain mechanism. Metal induced gap states (MIGS) could play a role in the interface trapping, however similar photoconductive gain has been established for other Schottky metals, such as Au,  $^{22}$  Pt,  $^{23}$  Ti,  $^{24}$  and other orientations of  $\beta\text{-Ga}_2\text{O}_3$ , such as (100),  $^{22}$  (010).  $^{23}$  It seems unlikely that MIGS could play a similar role in all such scenarios. However, STHs as initially theorized by Armstrong et al.  $^{19}$ , and further observed in other  $\beta\text{-Ga}_2\text{O}_3\text{-based photodetectors}, ^{20,21,24}$  have the means to provide photoconductive gain. In the case of the GO-1 Schottky, photoconductive gain is attributed due to the strong trapping at the 5 nm Ni contact.

Similar arguments can be espoused in the case of the InGO-1 MSM detector, as it also has high responsivity and slow time response. However, the SPCM indicates significant recombination in the device channel as well as both Schottky contacts. There is no established literature on gain mechanisms in  $\beta$ -(In<sub>x</sub>Ga<sub>1-x</sub>)<sub>2</sub>O<sub>3</sub> photodetectors, but results suggest that surface states in the channel and trapping at the Schottky interface, due to STHs, both play a role. In the channel, it can be speculated a high density of surface states within nanodomain boundaries act as negatively charged defects that bend energy bands upward. When illuminated, as in the case for Ga<sub>2</sub>O<sub>3</sub>, these surface states are filled and the barrier is lowered, resulting in higher photoconductivity. A similar effect is reported in ZnO nanowires.<sup>2</sup>

### CONCLUSIONS

In this study we characterized the orientation, compositions, and band gaps of  $\beta$ -phase (Al,Ga,In)<sub>2</sub>O<sub>3</sub> highly-oriented epitaxial films grown on (001) sapphire by MOCVD, and measured their performances as Schottky and MSM UV photodetectors. The calculated bandgaps were observed to vary over a range of  $\sim 1.5$  eV, as a function of

Characterization of Epitaxial  $\beta$ -(Al,Ga,In)<sub>2</sub>O<sub>3</sub>-Based Films and Applications as UV Photodetectors

composition. The resulting photodetectors, which includes the highest Al-content  $\beta$ -phase  $(Al_x-Ga_{1-x})_2O_3$  photodetector reported to date at  $X_{Al}=0.57\pm0.05$ , demonstrated low NEP and ultrahigh responsivities, which indicates the presence of photoconductive gain. The turn-on wavelengths for the photodetectors showed modest shifts ( $\sim 30$  nm) in accordance with the respective increase or decrease in the bandgaps of the films. The achievement of high photocurrents with such low incident light intensity opens up the possibility of using  $\beta$ -(Al,Ga,In)<sub>2</sub>O<sub>3</sub> materials as low-light sensing detectors.

#### ACKNOWLEDGMENTS

The authors would like to acknowledge support from the following sources: Department of Energy (DOE Contract # DE-SC0017885), National Science Foundation (Award # ECCS-1642740, supervised by Dr. Nadia El Masry and Dr. Paul Lane; and Award # ECCS-1711322, supervised by Dr. Paul Lane), and Army Research Office (program manager Michael Gerhold). The authors would like to acknowledge support from the University of South Carolina through the ASPIRE program. MLK acknowledges support from an NSF IGERT fellowship (Award #1250052). We'd like to thank Phillip Jean-Remy for helpful discussions regarding XPS analysis and Joshua Letton for his help measuring the devices at the University of South Carolina. We'd also like to thank Priscilla Chung for help with the AFM characterizations. Use of the Materials Characterization Facility at Carnegie Mellon University was supported by Grant MCF-677785.

#### REFERENCES

- K. Shimamura, E.G. Villora, K. Muramatu, K. Aoki, M. Nakamura, N. Ichinose, and K. Kitamura, J. Jpn. Assoc. Cryst. 33, 147 (2006).
- J. Zhang, C. Xia, Q. Deng, W. Xu, H. Shi, F. Wu, and J. Xu, J. Phys. Chem. Solids 67, 1656 (2006).
- G. Garton, S.H. Smith, and B.M. Wanklyn, J. Cryst. 13/14, 588 (1972).
- Y. Tomm, P. Reiche, D. Klimm, and T. Fukuda, J. Cryst. 220, 510 (2000).

- X. Wang, Z. Chen, F. Zhang, K. Saito, T. Tanaka, M. Nishio, and Q. Guo, *Ceram. Int.* 42, 12783 (2016).
- X. Wang, Z. Chen, F. Zhang, K. Saito, T. Tanaka, M. Nishio, and Q. Guo, AIP Adv. 6, 1 (2016).
- 7. S. Fujita and K. Kaneko, J. Cryst. 401, 588 (2014).
- 8. J. Tauc, Mater. Res. Bull. 3, 37 (1968).
- F. Zhang, K. Saito, T. Tanaka, M. Nishio, M. Arita, and Q. Guo, Appl. Phys. Lett. 105, 1 (2014).
- Y. Yao, L.A.M. Lyle, J.A. Rokholt, S. Okur, G.A. Tompa, T. Salagaj, N. Sbrockey, R.F. Davis, and L.M. Porter, ECS Trans. 80, 191 (2017).
- Y. Yao, S. Okur, L.A.M. Lyle, G.S. Tompa, T. Salagaj, N. Sbrockey, R.F. Davis, and L.M. Porter, *Mater. Res. Lett.* 6, 268 (2018).
- Y. Oshima, E. Ahmadi, S.C. Badescu, F. Wu, and J.S. Speck, Appl. Phys. Express 9, 6 (2016).
- F. Yang, J. Ma, C. Luan, and L. Kong, Appl. Surf. Sci. 255, 4401 (2009).
- W.Y. Weng, T.J. Hsueh, S.J. Chang, S.C. Hung, G.J. Huang, H.T. Hsueh, Z.D. Huang, and C.J. Chiu, *IEEE Sens. J.* 11, 1795 (2011).
- F. Zhang, K. Saito, T. Tanaka, M. Nishio, and Q. Guo, Solid State Commun. 186, 28 (2014).
- Q. Feng, X. Li, G. Han, L. Huang, F. Li, W. Tang, J. Zhang, and Y. Hao, Opt. Mater. Express 7, 4 (2017).
- F. Zhang, H. Li, M. Arita, and Q. Guo, Opt. Mater. Express 7, 10 (2017).
- K. Zhang, Q. Feng, L. Huang, Z. Hu, Z. Feng, A. Li, H. Zhou, X. Lu, C. Zhang, J. Zhang, and Y. Hao, *IEEE Photon. J.* 10, 1 (2018)
- A.M. Armstrong, M.H. Crawford, A. Jayawardena, A. Ahyi, and S. Dhar, J. Appl. Phys. 119, 1 (2016).
- X.C. Yang Xu, D. Zhou, F. Ren, J. Zhou, S. Bai, H. Lu, S. Gu, R. Zhang, Y. Zheng, and J. Ye, *IEEE Trans. Electron Devices* 66, 5 (2019).
- A.S. Pratiyush, S. Krishnamoorthy, S. Vishnu Solanke, Z. Xia, R. Muralidharan, S. Rajan, and D.N. Nath, Appl. Phys. Lett. 110, 1 (2017).
- R. Suzuki, S. Nakagomi, Y. Kokubun, N. Arai, and S. Ohira, Appl. Phys. Lett. 94, 1 (2009).
- 23. M. Kim, H.-C. Huang, J.D. Kim, K.D. Chabak, A.R.K. Kalapala, W. Zhou, and X. Li, *Appl. Phys. Lett.* 113, 1 (2018).
- B.R. Tak, M. Garg, S. Dewan, C.G. Torres-Castanedo, K.-H. Li, V. Gupta, X. Li, and R. Singh, J. Appl. Phys. 125, 1 (2019).
- Z.-M. Liao, K.-J. Liu, J.-M. Zhang, J. Xu, and D.-P. Yu, *Phys. Lett. A* 367, 207 (2007).

Publisher's Note Springer Nature remains neutral with regard to jurisdictional claims in published maps and institutional affiliations.